SANDIA REPORT
SAND2019-10870
Printed September 2019

Utilizing Highly Scattered Light for Intelligence through Aerosols

Brian Z. Bentz (PI), Brian J. Redman, Andres L. Sanchez, John D. Vander Laan, Karl Westlake, and Jeremy B. Wright

Prepared by
Sandia National Laboratories
Albuquerque, New Mexico 87185
Livermore, California 94550

Issued by Sandia National Laboratories, operated for the United States Department of Energy by National Technology & Engineering Solutions of Sandia, LLC.

Available to DOE and DOE contractors from

U.S. Department of Energy
Office of Scientific and Technical Information
P.O. Box 62
Oak Ridge, TN 37831

Telephone: (865) 576-8401
Facsimile: (865) 576-5728
E-Mail: reports@osti.gov
Online ordering: http://www.osti.gov/scitech

Available to the public from

U.S. Department of Commerce
National Technical Information Service
5301 Shawnee Road
Alexandria, VA 22312

Telephone: (800) 553-6847
Facsimile: (703) 605-6900
E-Mail: orders@ntis.gov
Online order: https://classic.ntis.gov/help/order-methods

ABSTRACT

This communication is the final report for the project Utilizing Highly Scattered Light for Intelligence through Aerosols funded by the Laboratory Directed Research and Development (LDRD) program at Sandia National Laboratories and lasting six months in 2019. Aerosols like fog reduce visibility and cause down-time that for critical systems or operations are unacceptable. Information is lost due to the random scattering and absorption of light by tiny particles. Computational diffuse optical imaging methods show promise for interpreting the light transmitted through fog, enabling sensing and imaging to improve situational awareness at depths 10 times greater than current methods. Developing this capability first requires verification and validation of diffusion models of light propagation in fog. For this reason, analytical models were developed and compared to experimental data captured at the Sandia National Laboratory Fog Chamber facility. A methodology was developed to incorporate the propagation of scattered light through the imaging optics to a pixel array. The diffusion approximation to the radiative transfer equation was found to predict light propagation in fog under the appropriate conditions.

This page intentionally left blank.

CONTENTS

LIST OF FIGURES

LIST OF TABLES

1. INTRODUCTION

Degraded visual environments (DVEs) are a major challenge for security and monitoring systems because situational awareness can be diminished or completely lost, limiting mission effectiveness. When the state of the environment can change in an unknown way it becomes difficult to manage risk and current solutions usually require costly actions. Aerosols that are naturally occurring or man-made can create DVEs that are sufficiently severe to impact security, transportation, aviation, remote sensing, surveillance, and more [1, 2, 3, 4, 5]. Fog is particularly concerning because it occurs in all climates and at certain locations with high frequency. Information is scrambled because the propagation direction of light in fog becomes randomized due to scattering from micron sized particles. Moreover, the light will be absorbed, leading to the loss of information. Therefore, in general, to maximize information transfer through fog for improved situational awareness, the scattered light must be deciphered, and the effect of absorption must be minimized.

In general, both scattering and absorption extinguish straight propagating or “ballistic” light, and the information it contains exponentially with depth [6]. This process is characterized by the mean free path l, which is the average distanced traveled by a photon between scattering and absorption events, and the transport mean free path l^*, which is the average distance over which a photon’s propagation direction becomes random. Both l and l^* depend on the wavelength of the light and the size and refractive index (RI) of the particles. In a dense aerosol or fog, l is about 1 m and l^* is about 10 m. Human visibility in this fog would not extend beyond 10 m.

To improve the situation, methods have been developed to reduce the effects of scatter and absorption on imaging. The methods generally discriminate two contributions to the light: first, the ballistic light that has traveled in a straight line from an object to a detector or lens system, and second, the scattered light that has changed propagation direction many times on the way to the detector. The ballistic light contains much more information than the scattered light and can form a high-resolution image of an object if the scattered light is rejected. For example, polarizing filters can reject scattered light that is in a different polarization state than the source light [7, 8, 9, 10]. Similarly, gated imaging methods can selectively detect ballistic photons by measuring the travel time of light pulses [11, 12, 13]. However, because the intensity of ballistic light decays exponentially with depth, the signal-to-noise ratio (SNR) falls rapidly, and images can only be formed up to depths of between l and l^*. Alternatively, both the ballistic and scattered photons could be used to form an image, enabling sensing and imaging to depths of perhaps at least $10l^*$ [1].

Coherent imaging methods have been developed that take advantage of the wave nature of light and the random interference of waves that have traveled different paths within the scattering media with each other. For example, the coherent intensity pattern of light transmitted through scattering media is called a speckle pattern, and this pattern and its correlations can be exploited for imaging [14, 15, 16]. However, these methods may be challenging to implement in aerosols because they are sensitive to moving particles. Alternatively, incoherent methods that do not take advantage of the wave nature of light could be naturally insensitive to particle motion in fog. For example, diffuse optical imaging (DOI) methods generally rely on computational imaging to invert a model that describes the propagation of photons in a scattering media [17]. Through optimization techniques [18, 19], it becomes possible to detect objects [20], estimate the locations of objects [21, 22] and even recover the shape of objects [18, 19, 23, 24]. DOI methods suffer relatively low spatial resolution because the coherent information is not used. However, for applications related to improving situational awareness and physical security, we expect the resolution of incoherent methods to be sufficient to locate and identify threats.

A first step in developing DOI methods for aerosols is to verify and validate the models of light propagation in fog. To this end, experiments were performed at the Sandia National Laboratory Fog Chamber facility (SNLFC), which can generate a repeatable and well characterized natural fog [25]. In Section 2, the light propagation models and the diffusion approximation are described. Analytical solutions are derived to be compared to experimental results. In Section 3, the relevant optical parameters of fog and corresponding model simulations are presented. In Section 4, a camera measurement model is presented that allows projection of the light scattered within a volume of fog to the pixel array. This measurement model allows comparison of images captured within the fog with model predictions. The experimental setup is described in Section 5, the results are presented in Section 6, and we conclude in Section 7.

2. MODELS

2.1. Radiative Transfer Equation

Propagation of electromagnetic waves in scattering media can be described by the radiative transfer equation (RTE) [17]

$$\frac{1}{c}\frac{\partial}{\partial t}I(\mathbf{r},t,\hat{\mathbf{s}})+\nabla\cdot I(\mathbf{r},t,\hat{\mathbf{s}})\hat{\mathbf{s}}+(\mu_a+\mu_s)I(\mathbf{r},t,\hat{\mathbf{s}})=\mu_s\int_{4\pi}f(\hat{\mathbf{s}},\hat{\mathbf{s}}')I(\mathbf{r},t,\hat{\mathbf{s}})d\Omega+Q(\mathbf{r},t,\hat{\mathbf{s}}) \tag{1}$$

where $\mathbf{r}$ denotes the position, c is the speed of light in the medium, $I(\mathbf{r},t,\hat{\mathbf{s}})$ (W/m^2/s/sr) is the radiance at time t in direction $\hat{\mathbf{s}}$, $\mu_a=\sigma_a n$ (m^{-1}) is the absorption coefficient, $\mu_s=\sigma_s n$ is the scattering coefficient (m^{-1}), σ_a is the absorption cross section (m^2), σ_s is the scattering cross section (m^2), n is the particle density (cm^{-3}), $l=1/(\mu_s+\mu_a)$, $f(\hat{\mathbf{s}},\hat{\mathbf{s}}')$ is the scattering phase function from incidence direction $\hat{\mathbf{s}}'$ to scattering direction $\hat{\mathbf{s}}$, and $Q(\mathbf{r},t,\hat{\mathbf{s}})$ (W/m^3/s/sr) is the radiance source term. The RTE provides an incoherent model that treats light as particles undergoing elastic collisions within a medium where interference effects are assumed to average to zero. Integrating over solid angle results in a continuity equation

$$\frac{1}{c}\frac{\partial}{\partial t}\phi(\mathbf{r},t)+\nabla\cdot\mathbf{J}(\mathbf{r},t)+\mu_a\phi(\mathbf{r},t)=S(\mathbf{r},t) \tag{2}$$

where $\phi(\mathbf{r},t)=\int_{4\pi}I(\mathbf{r},t,\hat{\mathbf{s}})d\Omega$ is the fluence rate (W/m^2/s), $\mathbf{J}(\mathbf{r},t)=\int_{4\pi}I(\mathbf{r},t,\hat{\mathbf{s}})\hat{\mathbf{s}}d\Omega$ is the flux density (W/m^2/s), and $S(\mathbf{r},t)=\int_{4\pi}Q(\mathbf{r},t,\hat{\mathbf{s}})d\Omega$ is the source (W/m^3/s).

2.2. Diffusion Equation

When the light within the medium experiences many more scattering events than absorption events ($\mu_s >> \mu_a$), the radiance can be expressed as the sum of an isotropic fluence rate ϕ and a small flux density $\mathbf{J}$, resulting in Fick's law [26]

$$\mathbf{J}(\mathbf{r},t) = -D\Delta\phi(\mathbf{r},t), \tag{3}$$

where the diffusion coefficient $D = 1/[3(\mu_s' + \mu_a)]$, $\mu_s' = \mu_s(1-g)$ is the reduced scattering coefficient, g is the average cosine of the scattering angle, or the anisotropy parameter, and $l^* = 1/(\mu_s' + \mu_a)$. As g decreases from 1, the light becomes less forward scattered. Plugging (3) into (2), the result is the diffusion equation (DE) [27]

$$\frac{1}{v}\frac{\partial}{\partial t}\phi(\mathbf{r},t) - \nabla\cdot[D(\mathbf{r})\nabla\phi(\mathbf{r},t)] + \mu_a(\mathbf{r})\phi(\mathbf{r},t) = S(\mathbf{r},t). \tag{4}$$

The solution to the DE is

$$\phi(\mathbf{r},t) = \int g(\mathbf{r},\mathbf{r}',t) * S(\mathbf{r}',t)d\mathbf{r}', \tag{5}$$

where $g(\mathbf{r},\mathbf{r}',t)$ is a Green's function to be determined and $*$ signifies a temporal convolution. If the medium is homogeneous with constant D and μ_a, and $S(\mathbf{r}',t) = S_o\delta(\mathbf{r}_s,t)$, where $\mathbf{r}_s$ is the location of a point source with power S_o (W) and δ is the Dirac delta function, the temporal analytic Green's function solution to the DE is [28]

$$\phi(\mathbf{r},t) = \frac{S_o c}{(4\pi Dct)^{3/2}}\exp\left(\frac{-|\mathbf{r}-\mathbf{r}_s|^2}{4Dct} - \mu_{a_m}ct\right). \tag{6}$$

Taking the Fourier transform of (4) with $\exp(j\omega t)$ time dependence results in the frequency domain form of the DE

$$\nabla\cdot[D(\mathbf{r})\nabla\phi(\mathbf{r},\omega)] - [\mu_a(\mathbf{r}) + j\omega/c]\,\phi(\mathbf{r},\omega) = -S(\mathbf{r};\omega), \tag{7}$$

where the fluence rate $\phi(\mathbf{r},\omega)$ has units of W/m^2. In a homogeneous medium and far from the source (7) simplifies to a scalar wave equation

$$\nabla^2\phi(\mathbf{r},\omega) + k^2\phi(\mathbf{r},\omega) = 0, \tag{8}$$

where $k^2 = (-\mu_a c - j\omega)/(Dc)$ is the wave number squared, and the solution,

$$\phi(\mathbf{r},\omega) = \left(\frac{S_o}{4\pi D}\right)\frac{\exp(-jk|\mathbf{r}-\mathbf{r}_s|)}{|\mathbf{r}-\mathbf{r}_s|}, \tag{9}$$

is the temporal Fourier transform of (6) and describes the propagation of what have been called diffuse photon density waves (DPDW's) [29]. The modulation frequency ω is on the order of

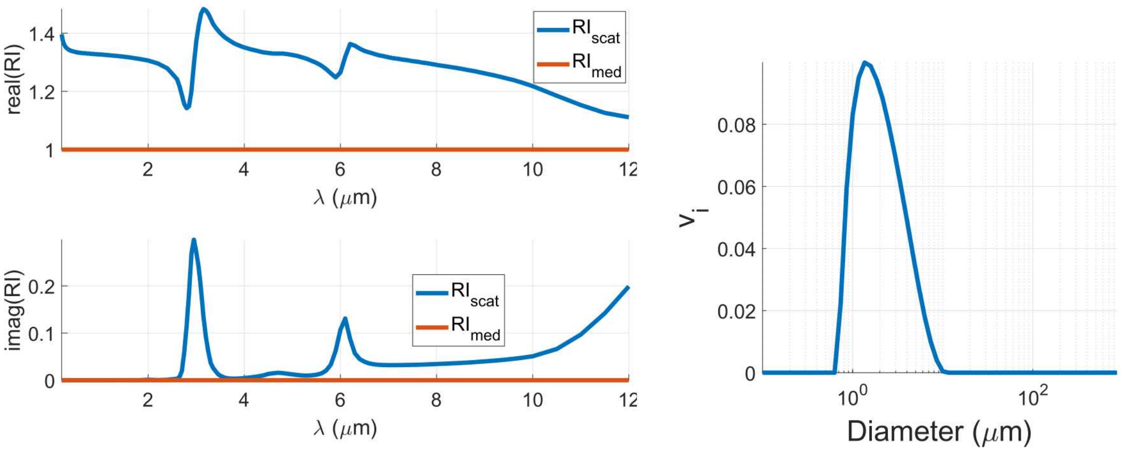

(a) (b)

Figure 3-1 Parameters used for simulation studies. (a) Real and imaginary parts of the refractive index (RI) of the scattering particle (water) and the background (free space). (b) Particle size distribution measured at the SNLFC.

MHz, and for the case of continuous wave or unmodulated ($\omega = 0$) light, (9) simplifies to

$$\phi(\mathbf{r}) = \left(\frac{S_o}{4\pi D}\right)\frac{\exp(\sqrt{\frac{\mu_a}{D}}|\mathbf{r}-\mathbf{r}_s|)}{|\mathbf{r}-\mathbf{r}_s|}. \tag{10}$$

In Section 3, the temporal and spatial analytic solutions to the diffusion equation, (6) and (10), are simulated with optical properties representative of fog, and in Section 6, (10) is compared to experimental measurements.

3. LIGHT PROPAGATION IN FOG

Interest at Sandia in imaging through and characterizing fog engendered the creation of one of the world's largest fog chambers in 2015 in Albuquerque, New Mexico [30]. At 3 x 3 x 55 m, the SNLFC provides a unique capability for sensor testing and the development of imaging methods in realistic fog conditions. To characterize the fog, a transmissometer measures the exponential attenuation of ballistic light and a particle sizer measures the size distribution of the fog water particles to determine l and l^* [25]. This characterization of the fog is ideal for verification and validation of models that describe light transport in scattering media. In this section we present simulations of the temporal and spatial solutions to the diffusion equation using the optical properties of the fog generated at the SNLFC.

3.1. Fog Optical Properties

Mie's solution to Maxwell's equations describes the scattering of a plane wave in a homogeneous medium by a sphere of known diameter and refractive index (RI) [31, 32]. The fields are written as an expansion in vector spherical harmonics, and coefficients describing the amplitudes of the scattered and internal fields can be calculated from the boundary conditions. The scattering and absorption efficiencies, Q_{sca} and Q_{abs}, as well as the anisotropy, g, can be written in terms of these coefficients. Assuming the spheres are far apart, $\mu_s = Q_{sca}An$ and $\mu_a = Q_{abs}An$, where $A = \pi(d/2)^2$ is the cross-sectional area of a sphere with diameter d, and n is the density of spheres (cm^{-3}). In fog, the spheres will have a distribution of diameters, d_i, where were i denotes a parameter of the ith sphere. We then find that

$$\mu_s = \frac{3}{2} f_v \sum_i \frac{Q_{sca_i} v_i}{d_i} \tag{11}$$

$$\mu_a = \frac{3}{2} f_v \sum_i \frac{Q_{abs_i} v_i}{d_i} \tag{12}$$

$$\mu_s' = \frac{3}{2} f_v \sum_i \left(\frac{Q_{sca_i} v_i}{d_i} \right) (1 - g_i), \tag{13}$$

where f_v is the particle volume fraction and v_i is the percent of the total volume contributed by particles of diameter d_i.

We simulate fog optical properties using the RI and particle size distribution of Fig. 3-1. Figure 3-1(a) shows the real and imaginary parts of the RI of the sphere that is scattering light (water) and the background medium (assumed to be free space) as functions of wavelength λ. Figure 3-1(b) shows a particle size distribution measured at the SNLFC. Most particles have diameters less than 10 μm, which is typical of a radiation fog. Radiation fog commonly forms overnight above ground that is cooling by thermal radiation [10]. As the air temperature drops below the dew point, water vapor changes to a liquid state and forms microscopic spheres that remain suspended in the air due to collisions with gas molecules. The thermodynamics of the droplet formation is described by Köhler theory [33], which allows prediction of droplet radius as a function of concentration of dissolved solute under conditions of supersaturation [34].

The simulated fog optical properties calculated for different particle densities n are shown in Fig. 3-2. As the wavelength is increased, the amount of scattering decreases, the light becomes less forward scattered, and the amount of absorption increases. Peaks in absorption corresponding to the resonances in Fig. 3-1(a) are observed at 2.95 μm and 6.1 μm. Two regions are found where $\mu_s > \mu_a$ and the diffusion approximation used to derive (4) applies. The first is at wavelengths between 200 nm and 2.7 μm, and the second is at wavelengths between 3.4 μm and 5.6μm. At wavelengths outside of these two regions, the RTE must be applied to model the light propagation.

Additional optical parameters of interest are the optical depth or thickness [10]

$$\tau = (\mu_s + \mu_a)L, \tag{14}$$

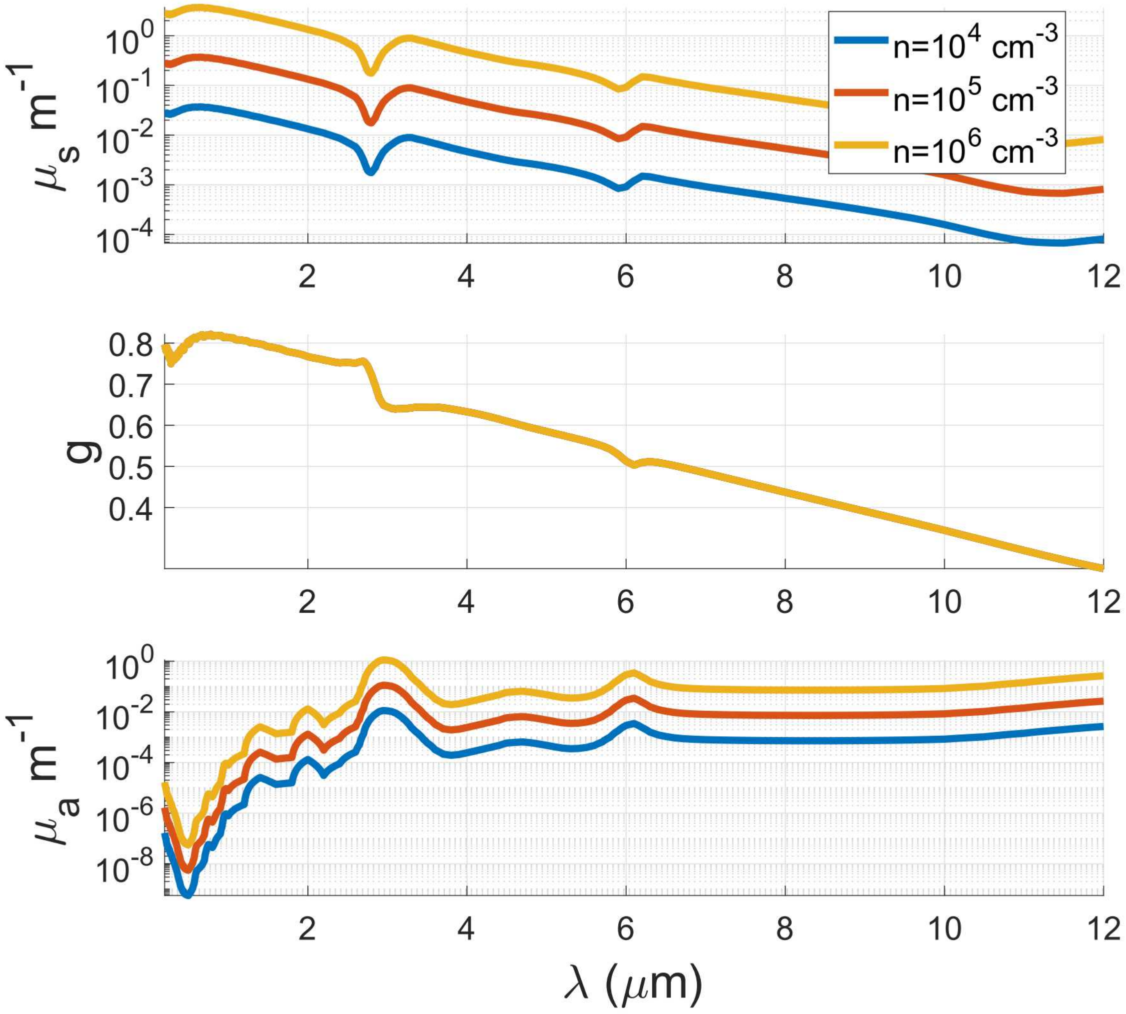

Figure 3-2 Fog optical properties simulated using Mie theory for different representative particle densities n using the parameters in Fig. 3-1.

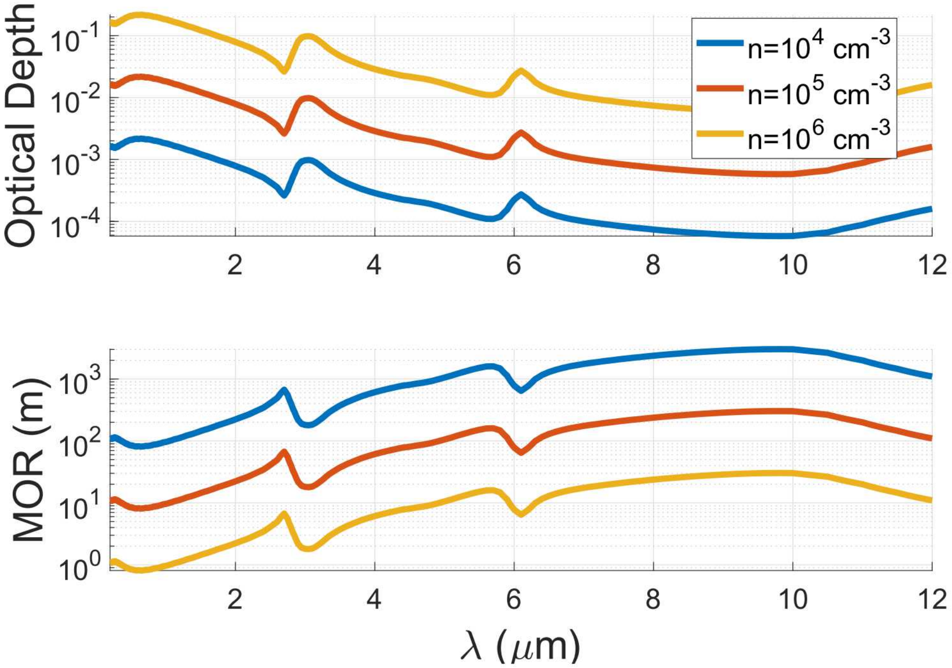

Figure 3-3 Optical depth τ calculated using $L = 5.8$ m and meteorological optical range (MOR) calculated using the parameters in Fig. 3-2.

where L is the distance between a source of light and a detector in homogeneous fog. Then, the attenuation of ballistic light is given by the Beer-Lambert law

$$\phi(L) = \phi_o \exp(-\tau), \tag{15}$$

where ϕ_o is the fluence rate at the source of light. The meteorological optical range (MOR), an approximation of human visibility, is given by

$$MOR = -\frac{\ln(0.05)}{\mu_s + \mu_a}. \tag{16}$$

Using τ and the Beer-Lambert law or MOR, distances in dense fogs generated at the SNLFC can be converted to equivalent distances in less dense fogs [25].

The optical depth and MOR are simulated in Fig. 3-3 using the parameters in Fig. 3-2 and $L = 5.8$ m (the experimental distance). The general trend is a decrease in optical depth and an increase in MOR with wavelength. While the MOR is not strictly defined for wavelengths outside the human visual range, it is useful for understanding the transmission of information through fog. In general, more information is transferred at higher wavelengths, even though the amount of absorption is increased. We also calculate the liquid water content (LWC), LWC = $f_v \rho_{water}$, where $\rho_{water} \approx 1$ g/cm^3 is the density of water, as 0.13 g/cm^3 when $n = 10^5$ cm^{-3}.

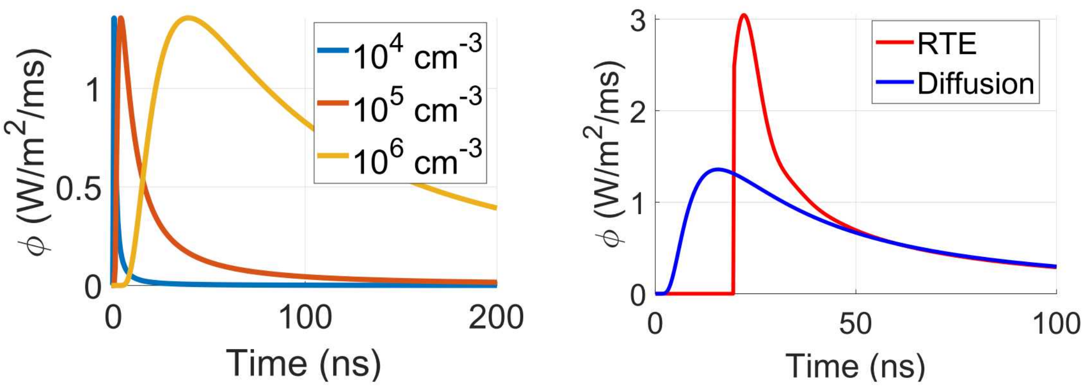

(a) (b)

Figure 3-4 Light propagation simulations of temporal solutions using fog parameters relevant to the experiment. (a) DE's temporal analytical Green's function solution for different fog densities. (b) Comparison of the RTE and DE temporal analytical Green's function solutions.

3.2. Simulations

We use fog optical properties from Fig. 3-2 that are relevant to the experiment to simulate analytical solutions to the DE. First, the time-domain solution (6) is considered. Assuming $L = 5.8$ m and light at $\lambda = 543$ nm, the DE's temporal analytic Green's function solution is calculated for different particle densities and plotted in Fig. 3-4(a). As the fog density is increased, the light experiences more scattering events, causing more photons to arrive at later times. The DE's solution is compared to the RTE analytic solution [35] in Fig. 3-4(b). The DE does not accurately describe the early arriving and nearly ballistic photons. For this reason, the temporal DE's solution may have limited utility in fog.

Next, the spatial-domain solution (10) is considered in Fig. 3-5. We consider only the unmodulated ($\omega = 0$) case, which is equivalent to the DC component or the integral of (10) over time. Light at $\lambda = 543$ nm and a fog density of 10^5 cm^{-3} were assumed, giving from Fig. 3-2, $\mu_s = 0.36$ m^{-1}, $g = 0.8$, and $\mu_a = 9.1 \times 10^{-9}$ m^{-1}. A 543 nm isotropic source, $S(\mathbf{r}', \omega) = S_o \delta(\mathbf{r}_s)$, is located at $\mathbf{r}_s = (x, y, z) = (0, 0, -0.02)$ m with $S_o = 200$ mW. The DE's spatial analytic Green's function solution is shown in Fig. 3-5(a), and the RTE spatial analytic Green's function solution is shown in Fig. 3-5(b). We see that, compared to Fig. 3-4, the DE solution is very close to that of the RTE, suggesting the unmodulated DE spatial solution will be useful for studies in fog.

4. CAMERA MEASUREMENT

Cameras are ubiquitous and provide a high density of information that can be easily interpreted by the human visual system. When fog is present, the information is scrambled by light

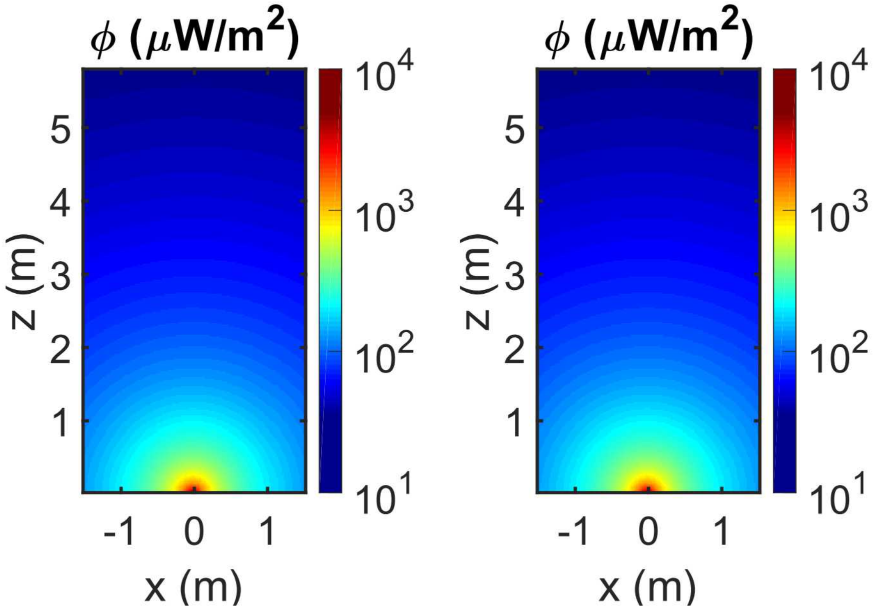

(a) (b)

Figure 3-5 Light propagation simulations of spatial solutions using fog parameters relevant to the experiment. An isotropic source is located at $\mathbf{r}_s = (0,0,-0.02)$ m. (a) DE's spatial analytical Green's function solution plotted in the $y = 0$ m xz plane. (b) RTE's spatial analytical Green's function solution plotted in the $y = 0$ m xz plane.

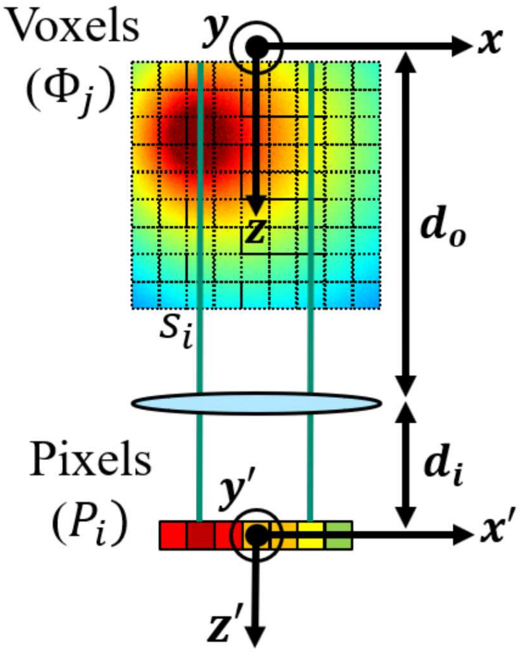

Figure 4-1 Projection of the flux within the jth voxel, ϕ_j, through the imaging system to the ith pixel, P_i. Each pixel will integrate the contribution along its line of sight, s_i. The distance from the pixel array to the lens, d_i, and the distance from the lens to the jth voxel, $d_o - z$, define the magnification and a coordinate transformation from (x, y, z) to (x', y', z').

scattering, motivating the need for computational methods that can translate the scrambled camera measurements into something that can be understood by a human being. However, light propagation from a source through fog and imaging optics to a detector or pixel array is a complex process. We have shown in Fig. 3-5 that a diffusion model can describe the propagation from a source through fog. Next, we describe a camera measurement model of the projection of light scattered within a volume of fog to a pixel array. The diffusion and camera measurement models are combined in software to interpret the experimental measurements.

Considering Fig. 4-1, our problem is to project light measured in the voxel or (x, y, z) space to the pixel or (x', y', z') space. This problem has been addressed using calibration methods in particle image velocity (PIV) or optical tomography [36], and we employ a similar method. The photon flux at the jth voxel position $\mathbf{r}_j$ due to source $S(\mathbf{r}_s)$ (assuming unmodulated light) from (5) is

$$\phi_j(\mathbf{r}_j) = \int g(\mathbf{r}_j, \mathbf{r}_s) S(\mathbf{r}_s) d\mathbf{r}_s. \tag{17}$$

The fluence rate measured by each pixel will be the integration along the pixel's line of sight of only the light that is not scattered on the way to camera aperture. Using the Beer-Lambert law (15), the ith pixel P_i at position $\mathbf{r}_i$ in (x',y',z') space will therefore measure

$$P_i(\mathbf{r}_i) = \int_{\mathbf{s}_i} \exp\left[-(\mu_s+\mu_a)|\mathbf{r}_j - \mathbf{r}_i|\right] \phi_j(\mathbf{r}_j) d\mathbf{s}_i, \tag{18}$$

where $\mathbf{s}_i$ is the pixel line of sight. For implementation on a computer, the volume must be discretized into voxels. The integration in (18) then becomes a summation and we write

$$P_i(\mathbf{r}_i) \approx \sum_j \mathbf{W} \exp\left[-(\mu_s+\mu_a)|\mathbf{r}_j - \mathbf{r}_i|\right] \phi_j(\mathbf{r}_j), \tag{19}$$

where $\mathbf{W}$ is a weighting matrix that represents the geometric contribution of each jth voxel to the ith pixel.

Populating $\mathbf{W}$ is considered a calibration step in PIV. In general, z' is always zero and

$$(x',y') = \mathbf{F}(x,y,z), \tag{20}$$

where $\mathbf{F}$ is a nonlinear function. $\mathbf{F}$ can be approximated with a least-squares polynomial, where the vector valued coefficients are estimated using experimental images of calibration targets [36]. This procedure has been shown to reduce or remove optical distortions along the imaging path, caused by, for example, glass-water interfaces in PIV. Since these distortions can be minimal when imaging in fog, we implement a simpler analytic solution to $\mathbf{F}$ that is based on the magnification principle. Considering the lens system of Fig. 4-1, where d_i is the distance from the lens to the pixel array and d_o is the distance from the lens to the furthest point within the volume of interest, the coordinate transformation is defined by

$$x' = \frac{-d_i}{d_o - z} x = -Mx \tag{21}$$

$$y' = \frac{-d_i}{d_o - z} y = -My, \tag{22}$$

where M is the magnification of the lens. If d_i and the pixel array dimensions of a camera system are known, (21) and (22) can be used to populate $\mathbf{W}$ for a user-defined discretized volume.

5. EXPERIMENT

To validate the models developed in Sections 3.2 and 4, an experiment was performed at the SNLFC. A schematic showing the experimental setup is shown in Fig. 5-1. Details of the fog generation are described elsewhere [34, 25]. Briefly, salt water solution was sprayed from 64 nozzles uniformly distributed along the length of the chamber. A Spraytec particle sizer from Malvern Instruments and a transmissometer provided the particle size distribution (v_i) and the particle density (n). The salt water was periodically sprayed in 25 minute cycles. During a cycle the fog density increases, and after the cycle is complete the fog density decreases. Throughout each cycle data was captured continuously by a visible CMOS camera (Basler acA2440) and the particle sizer and transmissometer, allowing camera images to be matched to the corresponding

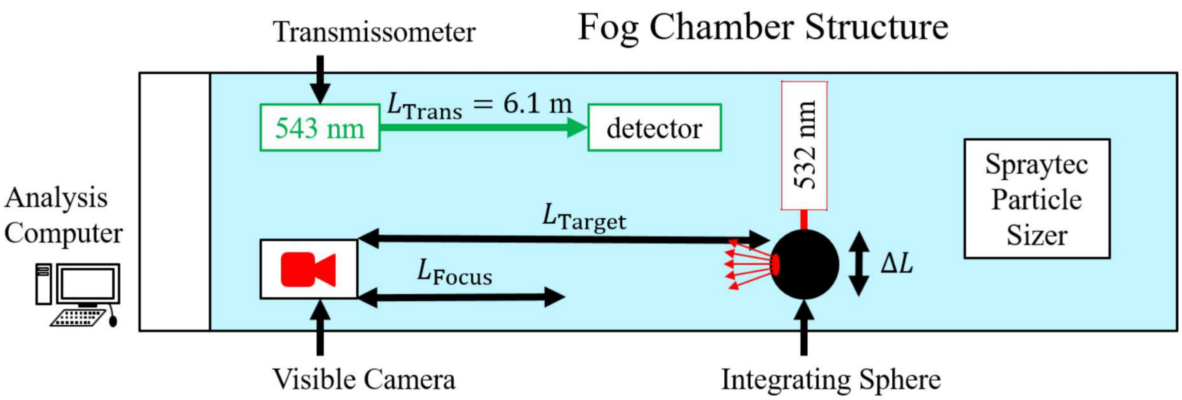

Figure 5-1 Experimental setup at the SNLFC. A transmissometer at 543 nm measures the light attenuation and a Spraytec particle sizer measures the particle size distribution. A visible camera is placed $L_{Target} = 5.8$ m from an integrating sphere emitting light at 532 nm. The camera was focused using a resolution target placed at $L_{Focus} = 1.4$ m. The integrating sphere could be translated side to side a distance ΔL.

fog optical parameters μ_s, g, and μ_a using (11), (12), and (13). The light source was a 532 nm, 200 mW laser incident on an integrating sphere (Thorlabs IS200-4). The output of the integrating sphere was directed towards the camera, and assumed to approximate an isotropic source for the purposes of verifying (10). The distance between the integrating sphere and the camera was 5.8 m, and the integrating sphere was translated a distance ΔL between fog spray cycles.

Photos of the experimental setup are shown in Fig. 5-2. Figure 5-2(a) shows the setup along the length of the SNLFC. The control computer is visible in the foreground, and the enclosures containing optical components are visible in the background. The transmissometer enclosures are on the right in the image and the camera and integrating sphere enclosures are on the left. The enclosures were maintained at slight positive pressure to prevent fog from entering. Figures 5-2(b) and (c) show photos of the integrating sphere radiation pattern from the front and side. Figures 5-2(d) and (e) show photos of a person holding a flashlight walking deeper into the fog. At increased depths, ballistic information is lost according to (15). Figure 5-2(f) shows the fog receding at the end of the test.

6. RESULTS

Here we compare the experimental measurements to the model predictions. First, (21) and (22) were used with $d_i = 5$ cm and $d_o = 5.8$ m to populate the weighting matrix $\mathbf{W}$. The free-space projection of the pixel positions (x', y', z') into (x, y, z) space was tested using images of a resolution target, and the results are presented in Fig. 6-1. The top row, Fig. 6-1(a)-(d), show raw image data of the resolution target at increasing distances from the camera. The x' and y' axes

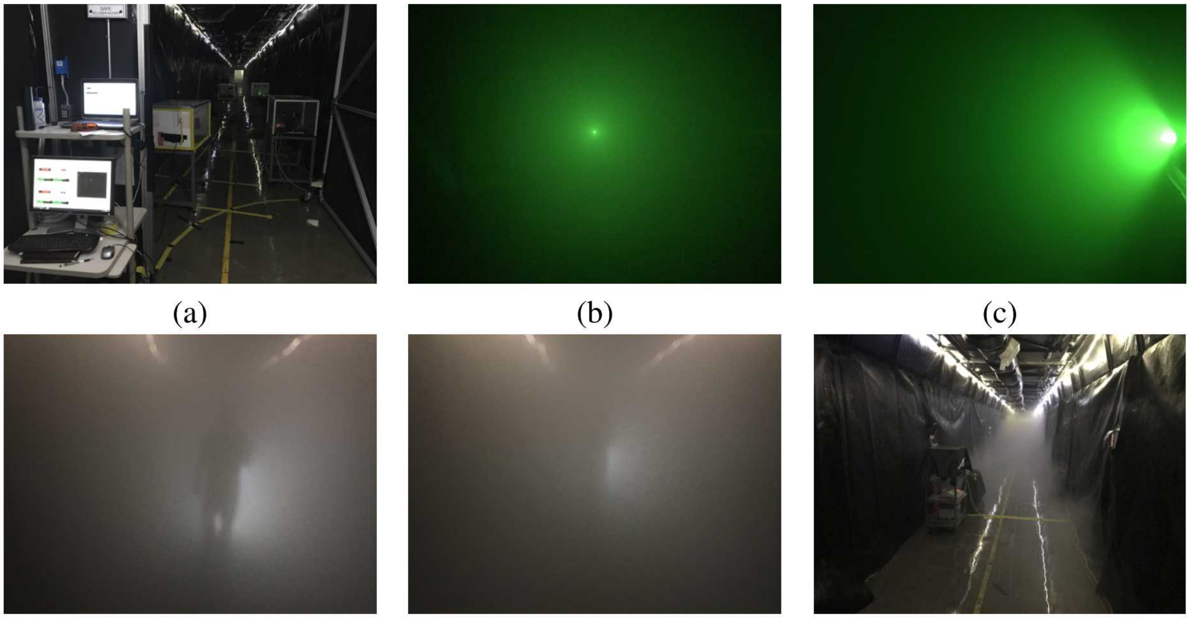

(a) (b) (c)

(d) (e) (f)

Figure 5-2 Photos of the experimental setup at the SNLFC. (a) Setup along length of the tunnel. (b) and (c) show photos of the integrating sphere radiation pattern from the front and side. (d) and (e) show photos of a person holding a flashlight walking deeper into the fog. (f) Fog receding at the end of the test.

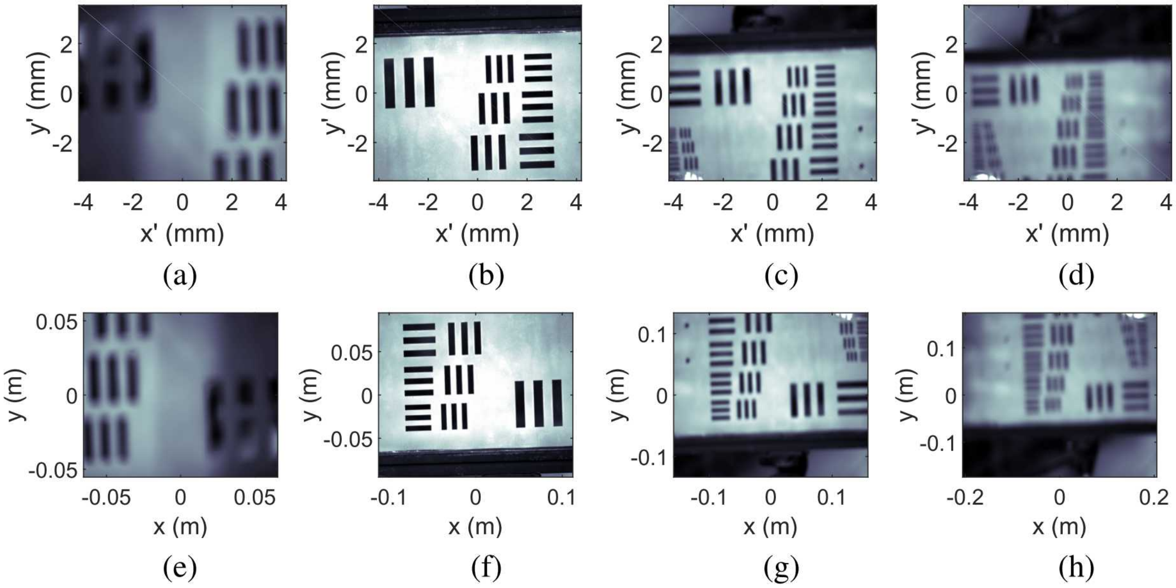

Figure 6-1 Demonstration of the projection from pixel to voxel space. Camera images were captured of a resolution plate at different depths (without fog present). (a), (b), (c), and (d) show pixel or (x', y', z') space images of the resolution target placed 0.8, 1.4, 1.9, and 2.5 m from the camera. Note that the pixel array was 8.4×7.1 mm. (e), (f), (g), and (h) show computed voxel or (x, y, z) space images, where $d_i = 5$ cm. The percent error was calculated between the known dimensions of the resolution target and the computed dimensions in these images as 8.3%, 2.8%, 1.2%, and 5.9%, respectively.

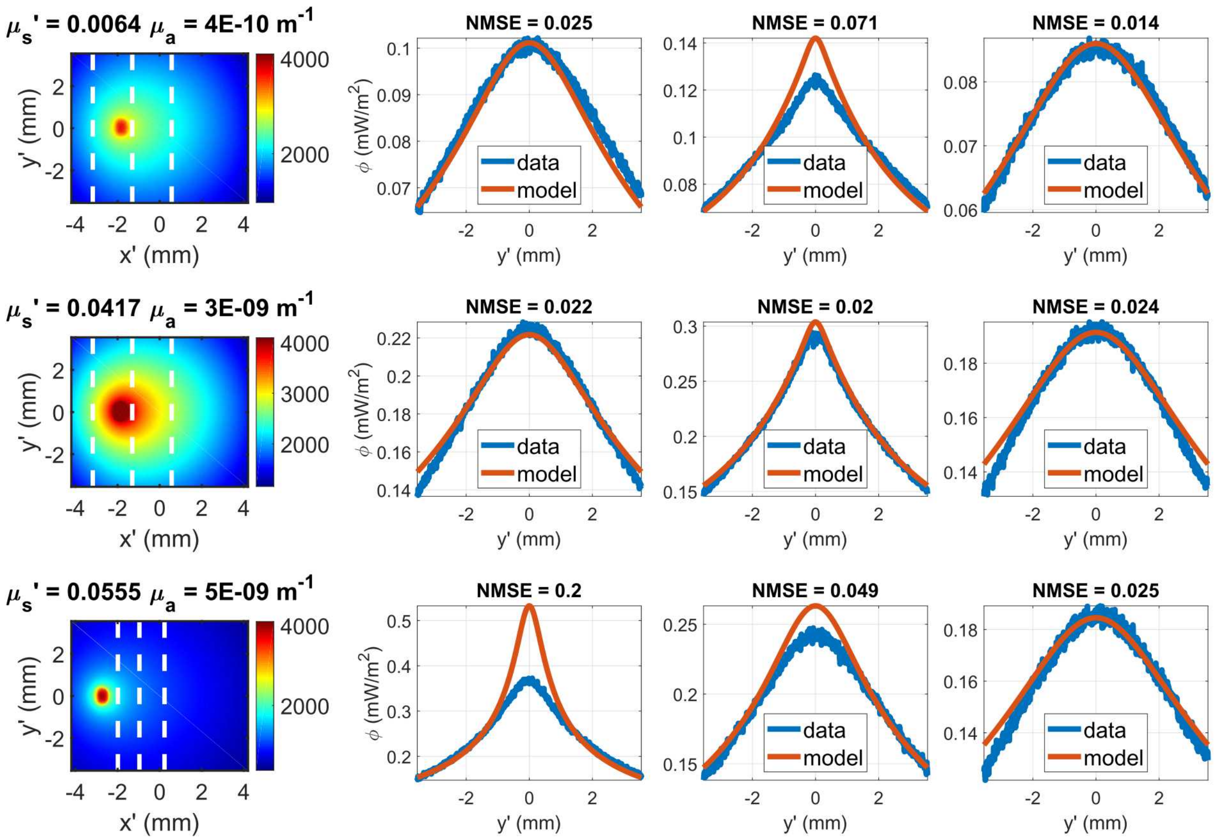

Figure 6-2 Modeling results using the DE's spatial analytical Green's function solution demonstrated in Fig. 3-5(a) and the voxel to pixel projection demonstrated in Fig. 6-1.

were defined by the number of pixels and the dimensions of the pixel array. The bottom row, Fig. 6-1(e)-(h), are the corresponding images of (a)-(d) projected into (x,y,z) space. The image is flipped because of the negative signs in (21) and (22). Using the known dimensions in the resolution target, the percent error in the predicted (x,y) coordinates of each image were calculated, and were 8.3%, 2.8%, 1.2%, and 5.9% for (e)-(h), respectively.

Finally, images were captured using the experimental setup shown in Fig. 5-1 to compare to (10) using the weighting matrix $\mathbf{W}$ from Fig. 6-1. The fog optical parameters μ_s, g, and μ_a were computed using (11), (12), and (13) and the transmissometer and particle sizer data. Representative results are presented in Fig. 6-2. The fog optical parameters μ_s' and μ_a are shown above the images in the left column. The plots to the right of each image compare measured data along the dashed white lines to the model predictions. The image counts were first converted to photons using the detector quantum efficiency and pixel saturation capacity. The photons measured by each pixel were then converted to energy (J), and finally to mW/m^2 using the detector integration time and the physical size of the pixel. Each data set was then scaled by a constant value close to 1 so that the spatial variation of the model and data could be compared. Future work will include a calibration step to determine this constant scaling factor. The plots from left to right correspond to the dashed white lines from left to right, respectively. To compare the measured and modeled data, we calculate the normalized mean square error (NMSE) [18]

$$\mathrm{NMSE} = \left\{ \frac{\sum_{k=1}^{N} [P_i^{mod}(\mathbf{r}_{i_k}) - P_i^{exp}(\mathbf{r}_{i_k})]^2}{[P_i^{exp}(\mathbf{r}_{i_k})]^2} \right\}^{1/2}, \tag{23}$$

where $P_i^{mod}(\mathbf{r}_{i_k})$ is the model predicted pixel value, $P_i^{exp}(\mathbf{r}_{i_k})$ is the experimentally measured value, and k is an index from 1 to N of the pixel positions $\mathbf{r}_i$ used for the comparison.

In the first two rows of Fig. 5-1, $\Delta L = 0$, however the integrating sphere was tilted slightly, causing the image data to be skewed to the left. Nevertheless, the model still provides a good prediction of the measured data. The prediction is not as good in the high intensity region, and this discrepancy may be due to the approximation of the integrating sphere as an isotropic source. This is supported by the data in the second row, where μ_s' has increased by almost ten times, and the integrating sphere more closely resembles an isotropic source. In the third row of Fig. 5-1, $\Delta L = 7.6$ cm, and we see that this translation has a substantial impact on the data. The NMSE is large for the data in the high intensity region, and we expect this discrepancy is also due to inaccurate modeling of the tilted integrating sphere. Follow up experiments are planned to address this discrepancy. Numerical solutions based on the finite element method (FEM) [37] will be employed to better model sources like a tilted integrating sphere or an object reflecting light.

During a follow up experiment, it was discovered that the parameter setup of the Spraytec particle sizer from Malvern Instruments was being done incorrectly, causing the measured mean particle diameter to be too large by about 0.5 μm. This introduced an error into the values of μ_s' and μ_a displayed in the left column of Fig. 6-2 that contributed to the difference between model and experimental data.

7. CONCLUSION

Models of light propagation in fog were verified and validated using image data captured at the Sandia National Laboratory Fog Chamber facility. These initial modeling and experimental results suggest that the diffusion approximation to the radiative transfer equation can predict the light propagation. However, more sophisticated models are required to describe light propagation from sources that are not isotropic. Future work will include developing and verifying FEM models of diffuse light propagation and imaging illuminated and thermally emitting objects in fog. Improved calibration procedures will be considered for better formation of the weighting matrix **W**. Once the models have been developed and validated, computational sensing and imaging methods will be explored that invert the models to enable detection, localization, and imaging of objects in fog for improved situational awareness.

ACKNOWLEDGMENT

This research was supported by the Laboratory Directed Research and Development (LDRD) Program at Sandia National Laboratories. We thank Laura J. Lemieux and Steven Storch for their assistance operating the Sandia National Laboratory Fog Chamber facility. We thank Philip L. Dreike for the useful discussions and for acting as program manager.

REFERENCES

[1] Allard Mosk, Yaron Silberberg, Kevin Webb, and Changhuei Yang. Imaging, sensing, and communication through highly scattering complex media. Technical report, Defense Technical Information Center, 2015.

[2] I Gultepe, G Pearson, JA Milbrandt, B Hansen, S Platnick, P Taylor, M Gordon, JP Oakley, and SG Cober. The fog remote sensing and modeling field project. *Bulletin of the American Meteorological Society*, 90(3):341–360, 2009.

[3] Andrew J Fultz and Walker S Ashley. Fatal weather-related general aviation accidents in the United States. *Physical Geography*, 37(5):291–312, 2016.

[4] Walker S Ashley, Stephen Strader, Douglas C Dziubla, and Alex Haberlie. Driving blind: Weather-related vision hazards and fatal motor vehicle crashes. *Bulletin of the American Meteorological Society*, 96(5):755–778, 2015.

[5] Paul A Pisano, Lynette C Goodwin, and Michael A Rossetti. US highway crashes in adverse road weather conditions. In *24th Conference on International Interactive Information and Processing Systems for Meteorology, Oceanography and Hydrology, New Orleans, LA*, 2008.

[6] August Beer. Bestimmung der absorption des rothen lichts in farbigen flussigkeiten. *Ann. Physik*, 162:78–88, 1852.

[7] Zhenyu Wang, Mark A Webster, Andrew M Weiner, and Kevin J Webb. Polarized temporal impulse response for scattering media from third-order frequency correlations of speckle intensity patterns. *Journal of the Optical Society of America A*, 23(12):3045–3053, 2006.

[8] John D van der Laan, Jeremy B Wright, David A Scrymgeour, Shanalyn A Kemme, and Eustace L Dereniak. Evolution of circular and linear polarization in scattering environments. *Optics Express*, 23(25):31874–31888, 2015.

[9] John D van der Laan, Jeremy B Wright, David A Scrymgeour, Shanalyn A Kemme, and Eustace L Dereniak. Effects of collection geometry variations on linear and circular polarization persistence in both isotropic-scattering and forward-scattering environments. *Applied Optics*, 55(32):9042–9048, 2016.

[10] John D van der Laan, Jeremy Benjamin Wright, Shanalyn A Kemme, and David A Scrymgeour. Superior signal persistence of circularly polarized light in polydisperse, real-world fog environments. *Applied Optics*, 57(19):5464–5473, 2018.

[11] Nils H Abramson and Kenneth G Spears. Single pulse light-in-flight recording by holography. *Applied Optics*, 28(10):1834–1841, 1989.

[12] L Wang, PP Ho, C Liu, G Zhang, and RR Alfano. Ballistic 2-d imaging through scattering walls using an ultrafast optical Kerr gate. *Science*, 253(5021):769–771, 1991.

[13] Martin Laurenzis, Frank Christnacher, David Monnin, and Ingo Zielenski. 3D range-gated imaging in scattering environments. In *Laser Radar Technology and Applications XV*, volume 7684, page 768406. International Society for Optics and Photonics, 2010.

[14] EG Van Putten, D Akbulut, J Bertolotti, Willem L Vos, Aart Lagendijk, and AP Mosk. Scattering lens resolves sub-100 nm structures with visible light. *Physical Review Letters*, 106(19):193905, 2011.

[15] Ori Katz, Pierre Heidmann, Mathias Fink, and Sylvain Gigan. Non-invasive single-shot imaging through scattering layers and around corners via speckle correlations. *Nature Photonics*, 8(10):784, 2014.

[16] Qiaoen Luo, Jason A Newman, and Kevin J Webb. Motion-based coherent optical imaging in heavily scattering random media. *Optics Letters*, 44(11):2716–2719, 2019.

[17] Subrahmanyan Chandrasekhar. *Radiative Transfer*. Courier Corporation, 1960.

[18] Jong Chul Ye, Kevin J Webb, Charles A Bouman, and Rick P Millane. Optical diffusion tomography by iterative-coordinate-descent optimization in a Bayesian framework. *Journal of the Optical Society of America A*, 16(10):2400–2412, 1999.

[19] S. R. Arridge. Optical tomography in medical imaging. *Inverse Problems*, 15:R41–R93, 1999.

[20] Brian Z Bentz, Dergan Lin, Justin A. Patel, and Kevin J Webb. Multiresolution localization with temporal scanning for super-resolution diffuse optical imaging of fluorescence. *IEEE Transactions on Image Processing*, 2019.

[21] Brian Z Bentz, Timothy C Wu, Vaibhav Gaind, and Kevin J Webb. Diffuse optical localization of blood vessels and 3D printing for guiding oral surgery. *Applied Optics*, 56(23):6649–6654, 2017.

[22] Brian Z Bentz, Dergan Lin, and Kevin J Webb. Superresolution diffuse optical imaging by localization of fluorescence. *Physical Review Applied*, 10(3):034021, 2018.

[23] Esther HR Tsai, Brian Z Bentz, Venkatesh Chelvam, Vaibhav Gaind, Kevin J Webb, and Philip S Low. In vivo mouse fluorescence imaging for folate-targeted delivery and release kinetics. *Biomedical Optics Express*, 5(8):2662–2678, 2014.

[24] Brian Z Bentz, Anmol V Chavan, Dergan Lin, Esther HR Tsai, and Kevin J Webb. Fabrication and application of heterogeneous printed mouse phantoms for whole animal optical imaging. *Applied Optics*, 55(2):280–287, 2016.

[25] Brian J Redman, John D van der Laan, Karl R Westlake, Jacob W Segal, Charles F LaCasse, Andres L Sanchez, and Jeremy B Wright. Measuring resolution degradation of long-wavelength infrared imagery in fog. *Optical Engineering*, 58(5):051806, 2019.

[26] Richard C Haskell, Lars O Svaasand, Tsong-Tseh Tsay, Ti-Chen Feng, Matthew S McAdams, and Bruce J Tromberg. Boundary conditions for the diffusion equation in radiative transfer. *Journal of the Optical Society of America A*, 11(10):2727–2741, 1994.

[27] James J Duderstadt and Louis J Hamilton. *Nuclear Reactor Analysis*. Ann Arbor, Michigan: Wiley-Interscience, 1976.

[28] Michael S Patterson, Britton Chance, and Brian C Wilson. Time resolved reflectance and transmittance for the noninvasive measurement of tissue optical properties. *Applied Optics*, 28(12):2331–2336, 1989.

[29] J Ripoll, M Nieto-Vesperinas, and Rémi Carminati. Spatial resolution of diffuse photon density waves. *Journal of the Optical Society of America A*, 16(6):1466–1476, 1999.

[30] Heather Clark. Fog on demand: Sandia-operated facility makes testing optics more cost-effective, efficient. *Sanida Lab news*, 2015.

[31] Craig F Bohren and Donald R Huffman. *Absorption and scattering of light by small particles*. John Wiley & Sons, 2008.

[32] Brian Z Bentz, Anna G Bowen, Dergan Lin, Daniel Ysselstein, Davin H Huston, Jean-Christophe Rochet, and Kevin J Webb. Printed optics: phantoms for quantitative deep tissue fluorescence imaging. *Optics Letters*, 41(22):5230–5233, 2016.

[33] Hilding Köhler. The nucleus in and the growth of hygroscopic droplets. *Transactions of the Faraday Society*, 32:1152–1161, 1936.

[34] Jeremy B Wright, John D van der Laan, Andres Sanchez, Shanalyn A Kemme, and David A Scrymgeour. Optical characterization of the Sandia fog facility. In *Degraded Environments: Sensing, Processing, and Display 2017*, volume 10197, page 1019704. International Society for Optics and Photonics, 2017.

[35] André Liemert and Alwin Kienle. Infinite space GreenâĂŹs function of the time-dependent radiative transfer equation. *Biomedical Optics Express*, 3(3):543–551, 2012.

[36] Steven M Soloff, Ronald J Adrian, and Zi-Chao Liu. Distortion compensation for generalized stereoscopic particle image velocimetry. *Measurement Science and Technology*, 8(12):1441, 1997.

[37] Martin Schweiger and Simon R Arridge. The Toast++ software suite for forward and inverse modeling in optical tomography. *Journal of Biomedical Optics*, 19(4):040801, 2014.

DISTRIBUTION

Hardcopy—Internal

Number of Copies	Name	Org.	Mailstop
5	Brian Z. Bentz	02585	0878
1	Brian J. Redman	06751	0937
1	Andres L. Sanchez	06633	1104
1	John D. Vander Laan	06751	0406
1	Karl Westlake	06788	0968
1	Jeremy B. Wright	06775	0968
1	Philip L. Dreike	06700	0966
1	D. Chavez, LDRD Office	1911	0359

Email—Internal [redacted]

Name	Org.	Sandia Email Address
Technical Library	01177	libref@sandia.gov

This page intentionally left blank.